Journal of Flow Visualization & Image Processing, x(x): 1–20 (2019)

MEASURING FLUID INTERFACES, CORNERS AND ANGLES FROM HIGH-SPEED DIGITAL IMAGES OF IMPACTING DROPS

D. Biolè[1] & V. Bertola[1,*]

[1]*Laboratory of Technical Physics, University of Liverpool, Liverpool, L69 3GH, United Kingdom*

*Address all correspondence to: V. Bertola, Laboratory of Technical Physics, University of Liverpool, Liverpool, L69 3GH, UK, E-mail: Volfango.Bertola@liverpool.ac.uk

Modern high-speed digital cameras enable the investigation of fluid flows with unprecedented resolution both in space and in time. A remarkable example is given by the study of drop impact and dynamic wetting phenomena, which occur on time scales of few milliseconds and exhibit features, such as the contact angle, which are often treated as geometric singularities. Whilst a good resolution of the camera sensor and a high-quality optics are obvious prerequisites to obtain accurate measurements, the extraction of quantitative information from digital images always requires some kind of processing algorithm. In particular, the accurate measurement of the position and velocity of fluid interfaces, and that of contact angles, require the identification of image features such as contours, edges and corners, which represents a non-trivial problem of digital image processing with fundamental applications in machine vision systems. This work illustrates systematic analytical procedures to identify fluid interfaces, corners and angles in high-speed digital images of fluid flows, with focus on their application to the study of drop impact and dynamic wetting phenomena.

KEY WORDS: *Drop impact, contact line, contact angle, image processing*

1. INTRODUCTION

The increasing accessibility of high-speed, high-resolution imaging systems enables the experimental study of fluid flows with unprecedented level of detail. These imaging systems produce large stacks of images with several megapixels resolution, increasing exponentially the amount of raw data generated during experiments. Thus, it is necessary to develop fast, reliable, consistent algorithms and procedures to obtain accurate quantitative measurements from digital images.

A remarkable example of a research topic that received great impulse from the systematic use of high-speed imaging is drop impact dynamics. When a liquid drop impacts onto solid substrate different outcomes may be observed (Rioboo et al., 2001), however all of these phenomena are characterized by very short characteristic times. Depending upon the impact Weber number, $We = \rho U^2 D_0/\sigma$ (where ρ is the fluid density, σ the surface tension, U the impact velocity,and D_0 the equilibrium drop diameter), the inertial spreading phase develops in about 5 ms, and the following receding phase in about 50 ms after maximum spreading; this means that at the frame rate of 5000 fps there are 25 images available for the analysis of the spreading phase and 250 images for the analysis of the receding phase.

1065–3090/17/$35.00

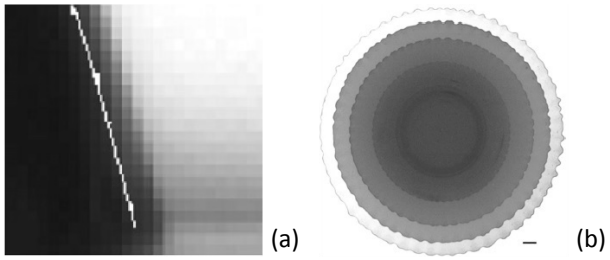

FIG. 1: (a) Example of inaccurate interface detection using the Canny algorithm (Chini and Amirfazli, 2011). (b) Visualization of the contact line at different times during dewetting (Thoroddsen and Sakakibara, 1998); the pixel intensity is non-monotonic (edge pixels are darker).

To analyse phenomena of such a short duration, different imaging devices and techniques are discussed in literature (Hutchings et al., 2007; Thoroddsen et al., 2008; Versluis, 2013). However, irrespective of the experimental technique used to acquire images, extracting quantitative features (e.g., lengths and/or angles) from drop impact experiments requires some sort of image processing, especially to identify contour lines with precision; unfortunately, with few exceptions the details of the image processing algorithms used are not disclosed.

The output of a digital camera device is represented by a sequence of images, or frames, in the form of discrete light intensity maps, where both the field of view of the artificial eye and the light intensity are discretized and treated as matrices of integers. Let then $L(x, y, z)$ be the light intensity in a Cartesian space: an image $I(x, y)$ can be defined as the surface representing the amount of light that can be collected from an ideal plane $z = z^*$ placed at the working distance of the lens; it immediately follows that $I(x, y) = L(x, y, z^*)$. In practice, the ideal infinite plane $z = z^*$ is bounded by the field of view of the lens, and its resolution is limited by the sensor of the camera; thus, if Δ_p is the dot pitch of the sensor (i.e., the true pixel width on the sensor), and X and Y are, respectively, the upper bounds of the planar region originating in the point $O = \{0, 0\}$ that can be visualized from the lens, the theoretical maximum available resolution of the device is $(X/\Delta_p) \times (Y/\Delta_p)$ pixels. Each pixel p represents a specific location in the image grid that can be identified by two discrete spatial coordinates $x_i = i\Delta_p$ and $y_j = j\Delta_p$, and the light intensity $I_{i,j} = I(x_i, y_j)$.

Fluid interfaces usually correspond to large image intensity gradients, therefore they are often identified by fitting the pixel intensity profile with a sigmoid (Canny, 1986) and setting the edge position in the sigmoid inflexion point. However, sigmoid fitting may not identify the interface accurately depending on the image histogram, as shown in Figure 1a (Chini and Amirfazli, 2011). In addition, this method is not suitable in the presence of small intensity gradients and/or non-monotonic intensity profiles, such as in the example displayed in Figure 1b (Thoroddsen and Sakakibara, 1998).

Corners and angles are formed at the intersection of edges; this is the case, for example, of the contact angle of liquid drops deposited on a surface, defined as the angle between the solid surface and liquid-air interface on the side of the liquid phase. A common approach to measure contact angles from side views of drops consists in fitting one or more analytical functions to the drop shape, or to a part of it, in the neighborhood of the contact (three-phase) point, and then taking the analytical tangent to the fitting curve. In the Axisymmetric Drop Shape Analysis method (ADSA), a solution of the Laplace equation is fitted to the drop shape by minimizing the error between the theoretical and observed drop boundaries (Hoorfar and Neumann, 2006; Rotenberg

et al., 1983). A limitation of ADSA and other similar methods is they require drop symmetry, which makes them unsuitable to measure contact angles of drops moving on an inclined surface, or drops impacting on a solid surface. An alternative approach consists in fitting polynomials to a small portion of the drop edge near the contact line (Bateni et al., 2003; Schuetter et al., 2006); these methods are very sensitive to the order of the fitting polynomial and to the local image resolution, although accuracy can be improved using sub-pixel resolution (Chini and Amirfazli, 2011). In addition, interpolating the contour with a polynomial can displace artificially the contact point (Biolè et al., 2016). A simple edge-fitting method for asymmetric drops uses piecewise continuous polynomial functions (B-splines) (Stalder et al., 2006); these curves can fit reasonably well any drop shape, provided suitable nodes are selected on the drop edge. However, since these optimum nodes are specified manually by the user, the method is impractical to analyse large stacks of images, for example those generated by high-speed imaging systems.

This paper describes systematic image processing algorithms to identify features in digital images, such as edges, interfaces and corners, and to extract quantitative measurements of lengths and angles. In particular, algorithms are specifically adapted to address common issues arising in the processing of high-speed images of drop impact phenomena, and to provide accurate measurements of contour lengths and contact angles.

2. IMAGE PRE-PROCESSING

2.1 Intensity histogram equalization

The histogram of an image is the non-normalized distribution of the light intensity I (which sometimes is confused with the image brightness); since both the visual plane and the light intensity measured on the plane are discretized, the resulting distribution is also discrete. Very often in high-speed imaging the recorded frames are dark, due to the short exposure time of the sensor to the incoming light or to non optimal illumination conditions, as shown in the example displayed in Figure 2a. As a consequence, the corresponding histogram is polarized in the dark field (see Figure 2c). A simple technique to enhance contrast (i.e., the gap between the minimum and the maximum intensity of an image, measured in intensity units) in a dark image is to threshold the image (bound the intensity field between two values, I_{min} and I_{max}) and then rescale intensity according to Eq. (1).

$$I_{e\,i,j} := \frac{I_{i,j} - I_{min}}{I_{max} - I_{min}} \quad , \quad \forall\, p_{i,j} \;=\; p(x_i, y_j) \tag{1}$$

The equalized histogram (Figure 2c) covers the entire range of intensities available, enhancing the image contrast (Figure 2b).

2.2 Background removal

Images often contain unnecessary information, therefore any unwanted features should be erased by removing the image background. The simplest technique that can be used to remove the background contribution from an image is the pixel-by-pixel subtraction of a reference image $I_0(x, y)$, containing only the undesired objects, from the initial image $I(x, y)$. If the normalized intensity difference is below a certain threshold, the pixel intensity is set equal to a constant (e.g., to the maximum value of brightness), otherwise it remains identical to the initial image (see Eq. 2).

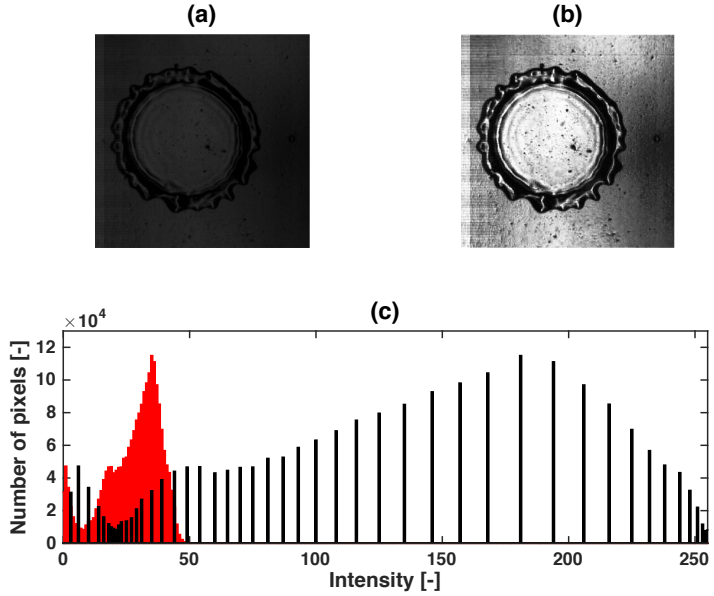

FIG. 2: Effect of histogram equalization. (a) Original image. (b) Image after histogram equalization. (c) Intensity histograms of the original image (red) and of the equalized image (black).

$$I_{c\,i,j} := \begin{cases} constant & \text{if } \left|\frac{I_{i,j}-I_{0\,i,j}}{I_{0\,i,j}}\right| < k \\ I_{i,j} & \text{otherwise} \end{cases} \quad , \quad \forall\, p_{i,j} \;=\; p(x_i, y_j) \tag{2}$$

More advanced techniques of background removal take into account the characteristics of the illumination sources, the materials properties, and the system geometry (Marr and Hildreth, 1980). For example, when back-to-front illumination with a coherent light source parallel to the optical axis of the camera is used, and there is no light scattering along the optical path, the image intensity results from light absorption according to Beer-Lambert law:

$$I(x, y) = I_0 \exp(-\lambda(x, y) z^*) \tag{3}$$

where I_0 is the (uniform) illumination intensity, $\lambda(x, y)$ is the absorption coefficient corresponding to the point (x, y), and z^* is the distance between the light source and the image plane. In this case, the ratio between the intensities of the initial image and of the reference image is an exponential function of the local light absorption coefficient (Eq. 4), therefore enhances the features of the initial image which are not present on the reference image. Thus, the background removal obtained using Eq. (4) yields a better result with respect to the background subtraction method.

$$I_{c\,i,j} := \frac{I_{i,j}}{I_{0\,i,j}} = \exp(-\lambda_{i,j}\, z^*) \quad , \quad \forall\, p_{i,j} \;=\; p(x_i, y_j) \tag{4}$$

Figure 3 shows the difference between background removal by subtraction (Figure 3b), and background removal by division (Figure 3c), for an image with back-to-front parallel illumination (Figure 3a).

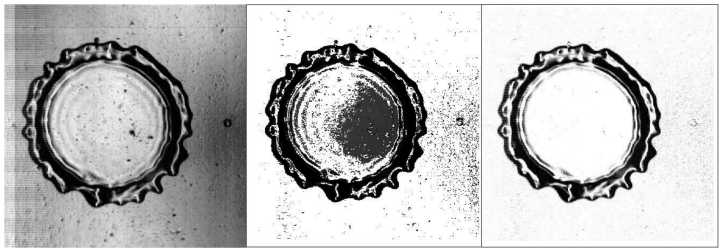

FIG. 3: (a) Original image. (b) Image after background removal (subtraction). (c) Image after background removal (division).

The main drawbacks that affect both algorithms are salt-and-pepper noise (i.e., small dots having high contrast with the background), and the formation of hot or cold spots (i.e., large regions with intensity that smaller than the lower bound or larger than the upper bound of the image class considered (for $8-bit$ integer unsigned images intensity in the range $[0, 255]$). Spatial averaging (filtering) is generaly sufficient to remove salt-and-pepper noise, while to mitigate hot or cold spots one can force the pixels intensity within the range admitted by the image class, changing the values over maximum and under minimum, or rescale all intensities between the maximum and minimum values defined by the highest-intensity hot-spot and the lowest-intensity cold-spot, respectively.

3. OBJECT IDENTIFICATION

3.1 Edge detection

Edge detection is one of the most fascinating topics in the history of computer vision (Canny, 1986; Lindeberg, 1996; Perona and Malik, 1990; Sobel and Feldman, 1968; Torre and Poggio, 1986). An edge represents the set of the pixel locations where the variation of the image intensity exceeds a prescribed threshold. Local changes of the intensity in an image may be caused by changes in illumination (shadows, visible light sources and illumination gradients), in the orientation or distance from the viewer to the visible surfaces, in surface reflectance (Marr and Hildreth, 1980) and any combination of them. Edge detection algorithms enhance the locations where the image intensity varies irrespective of the physical origin of this variation.

Most authors approach edge detection as the search of inflection points of one-dimensional functions; in fact, considering a smooth function $f(x)$ (twice continuous and differentiable on a sub-set of $\mathbf{R}$), its curvature (reciprocal of the gradient $f'(x)$) is minimum in correspondence of the zero-crossings of the second order derivative $f''(x) = 0$, therefore in these points the function $f(x)$ is expected to change rapidly. Unfortunately, extending this approach to surfaces or images is not straightforward. Given a smooth surface $S(x, y)$ (hence twice continuous and differentiable on $\mathbf{R}^2$), the information about how its shape changes over its domain is carried by its gradient, $\nabla S(x, y)$, its Hessian matrix, $H_S(x, y)$, and its Laplacian, $\Delta S(x, y)$, which represents the mean curvature in correspondence of the zero-crossings of the gradient. However, in most images the topology of the intensity map is not smooth at all, as shown in Figure 4a, which makes differentiation impossible. To obtain a differentiable surface, one can smooth the original image by applying a Gaussian filter using the integral operator of convolution:

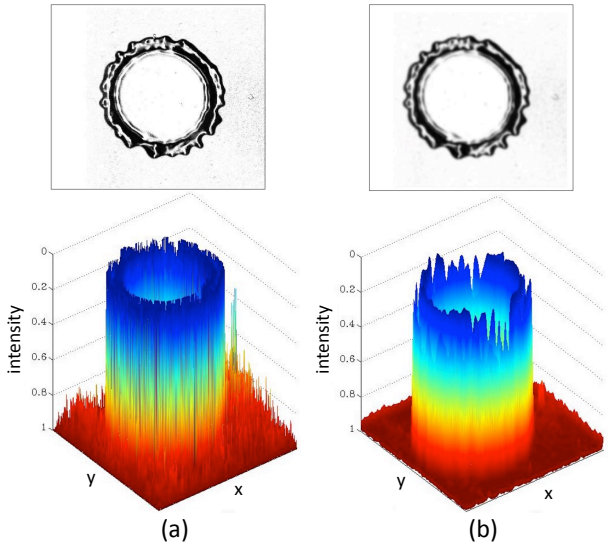

FIG. 4: Image intensity surface: (a) Original image; (b) The same image smoothed with a Gaussian filter with variance $\sigma_1 = 3$.

$$W(x, y, \sigma_1) = G(x, y, \sigma_1) * I(x, y) \tag{5}$$

An example of the effect of Gaussian smoothing is displayed in Figure 4b. Using the convolution properties, the intensity surface derivation can be calculated as:

$$\nabla W(x, y, \sigma_1) = \nabla G(x, y, \sigma_1) * I(x, y) = G(x, y, \sigma_1) * \nabla I(x, y) \tag{6}$$

The most common edge detection techniques based on image filtering are:

- Derivative of Gaussian (DoG): $\nabla W(x, y, \sigma_1) > k$
- Difference of Gaussians (doG): $|W(x, y, \sigma_1) - W(x, y, \sigma_2)| > k,\ \sigma_1 \neq \sigma_2$
- Laplacian of Gaussian (LoG): $\Delta W(x, y, \sigma_1) > k$

where k is a constant threshold value. The above inequalities are used to create synthetic binary images that are valued 1 only in the pixel locations where the constraint is verified, and zero otherwise. Figure 5 shows examples of edge detection on the same sample image using the Derivative of Gaussian (Figure 5a) and the Laplacian of Gaussian (Figure 5b) methods.

To reduce the computation time required to execute derivations, it was proposed to use small 3×3 kernels (Sobel and Feldman, 1968) for the partial derivatives in $||\nabla W|| = \sqrt{{W_x}^2 + {W_y}^2}$ and $\Delta W = W_{xx} + W_{yy}$ (where the terms $W_x = I * G_x, W_y = I * G_y, W_{xx} = I * G_{xx}, W_{yy} = I * G_{yy}$ represent the partial derivatives of the smoothed image). The general formula of a 3×3 derivation kernel can be written convolving the central difference scheme with a smoothing vector:

$$G_x = {G_y}^T = 2h\beta_1 \begin{bmatrix} 1 \\ b_1 \\ 1 \end{bmatrix} * \begin{bmatrix} -\frac{1}{2h} & 0 & \frac{1}{2h} \end{bmatrix} \tag{7}$$

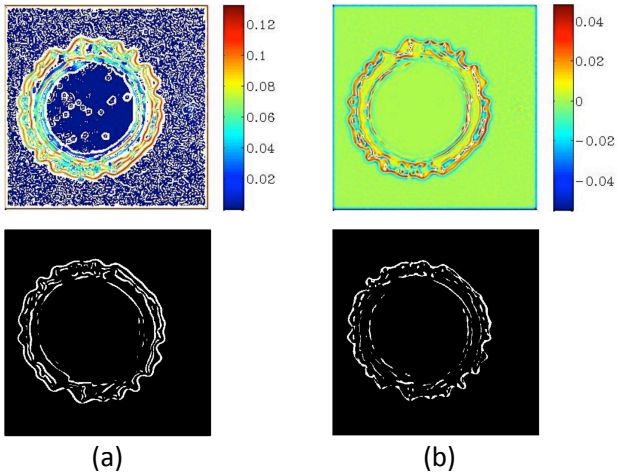

FIG. 5: Examples of differentiation of the smoothed sample image, and corresponding binary images. (a) intensity gradient $||\nabla W||$, used for the Derivative of Gaussian (DoG) method, with threshold $k = 0.08$; (b) Laplacian ΔW, used in the Laplacian of Gaussian method with threshold $k = 0.02$.

$$G_{xx} = {G_{yy}}^T = h^2 \beta_2 \begin{bmatrix} 1 \\ b_2 \\ 1 \end{bmatrix} * \begin{bmatrix} \frac{1}{h^2} & -\frac{b_2}{h^2} & \frac{1}{h^2} \end{bmatrix} \approx h^2 \beta_2 \begin{bmatrix} 1 \\ b_2 \\ 1 \end{bmatrix} * \begin{bmatrix} \frac{1}{h^2} & -\frac{2}{h^2} & \frac{1}{h^2} \end{bmatrix} \quad (8)$$

In the case of a Gaussian smoothed average the coefficients assume the following values: $\beta_1 = -(2\pi\sigma^3 e)^{-1}$, $b_1 = \sqrt{e}$, $\beta_2 = (\pi\sigma^4 e^3)^{-1}$, $b_2 = e\sqrt{e}$, and $h = 1$ for images.

More advanced edge detection algorithms identify edges as the zero crossing curves of differential invariants of a smooth and twice differentiable surface, such as the Lindeberg invariant (Lindeberg, 1993, 1998):

$$\mathcal{L} = W_x^2 W_{xx} + 2W_x W_y W_{xy} + W_y^2 W_{yy} \quad (9)$$

3.2 Corners detection

Corners are local features of images, usually represented using a very small subset of the image pixels. In the literature, corners are found either as intersection of two or more edges having different direction (i.e. a junction), or as points on lines (edges) where the local curvature is maximum (Mokhtarian and Suomela, 1998; Noble, 1987), or as points characterized by low self–similarity (Moravec, 1980).

Corner detection algorithms can be sorted into two main categories, i.e. algorithms based on contour curvature and algorithms based on image intensity. In algorithms based on contour curvature, corners lie on image edges, where the curvature along the chain of points describing an edge is calculated, and corners are identified in those pixels with either a large curvature or a large curvature gap from the neighboring points (Langridge, 1982; Rutkowski and Rosenfeld, 1978). In algorithms based on image intensity, corners are identified in regions with high mean curvature (Kitchen and Rosenfeld, 1982), therefore the search is not limited to edge lines, but covers the whole image surface.

Other methods look for intensity variations in fixed size windows. The Harris operator performs a local evaluation of the image autocorrelation and takes this quantity as a measure of the point self-similarity (Harris and Stephens, 1988). The SUSAN scheme (Smith and Brady, 1997) simply counts for every pixel the number of neighboring points having the same intensity, and does not perform any surface differentiation; local minima are taken as corner points.

From a mathematical point of view, a point $P = \{x_P, y_P\}$ belonging to an image $I(x, y)$ is a corner if it satisfies the following conditions:

- It belongs to the image edges, i.e., using Eq. (9), $\mathcal{L}(x_P, y_P) = 0$;
- The unit normal $\vec{n} = \nabla I/||\nabla I||$ to the surface in P is orthogonal to the unit normal $\vec{p} = \nabla\phi/||\nabla\phi||$ to the gradient of the surface inclination, defined as $\phi = \arctan(I_y/I_x)$.

Examples of the quantities ∇I and $\nabla\phi$ obtained from the image of a simple square corner are displayed in Figures 6a and 6b, respectively. In other words, corners can be defined as those edge points where $\vec{n} \cdot \vec{p} = 0$. This can be proven by showing that the conditions $L(x_P, y_P) = 0$ and $\vec{n} \cdot \vec{p} = 0$ correspond to points where the Gaussian curvature, κ, defined in Eq. (10), is maximum.

$$\kappa = \frac{I_{xx} I_{yy} - I_{xy}^2}{(1 + ||\nabla I||^2)^2} \tag{10}$$

The product $\vec{n} \cdot \vec{p}$ can be written as:

$$\vec{n} \cdot \vec{p} = \frac{\nabla I \nabla\phi}{||\nabla I||\,||\nabla\phi||} = \frac{I_x\phi_x + I_y\phi_y}{||\nabla I||\,||\nabla\phi||} = \cos\xi \tag{11}$$

where ξ is the angle between $\vec{n}$ and $\vec{p}$, and:

$$\phi_x = \frac{I_x(I_{xy} - I_{xx}\tan\phi)}{||\nabla I||^2} \tag{12}$$

$$\phi_y = -\frac{I_y(I_{xy} - I_{yy}\cot\phi)}{||\nabla I||^2} \tag{13}$$

Introducing Lindeberg's condition, $\mathcal{L} = 0$ (Eq. 9), yields:

$$I_{yy}\tan\phi - I_{xx}\cot\phi = 2||\nabla I||\,||\nabla\phi||\cos\xi \tag{14}$$

which can be re-written as:

$$I_{yy} = I_{xx}\frac{I_x^2}{I_y^2} + 2\frac{I_x}{I_y}||\nabla I||\,||\nabla\phi||\cos\xi \tag{15}$$

$$I_{xy} = -(\frac{I_x}{I_y}I_{xx} + ||\nabla I||\,||\nabla\phi||\cos\xi) \tag{16}$$

Introducing Eqs. (15) and (16) into the definition of Gaussian curvature, Eq. (10), yields:

$$\kappa = -\frac{||\nabla I||^2\,||\nabla\phi||^2}{(1 + ||\nabla I||^2)^2}(\cos\xi)^2 \tag{17}$$

Equation (17) shows that the maximum value of the Gaussian curvature is $\kappa = 0$, corresponding to $\xi = \pi/2$, i.e. the two unit vectors $\vec{n}$ and $\vec{p}$ are orthogonal, as shown in the example of Figure 6c relative to a square corner.

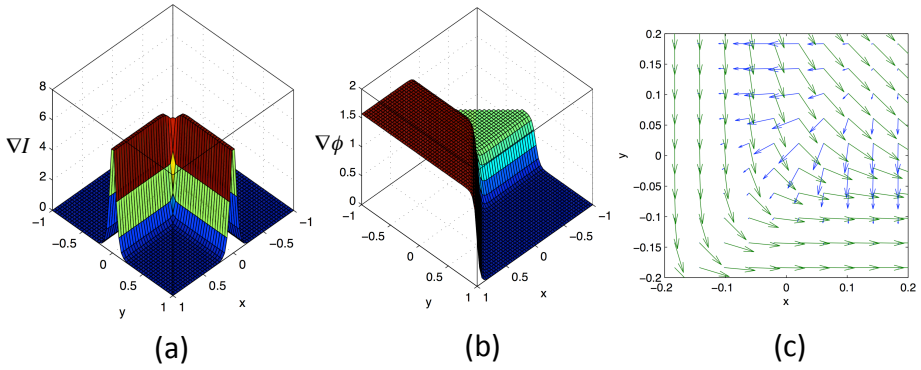

FIG. 6: Detection of a sample synthetic square corner: (a) intensity gradient ∇I; (b) gradient of the surface inclination $\nabla\phi$; (c) detail of the vector fields $\vec{n}$ (blue) and $\vec{p}$ (green) in the vicinity of the corner point.

4. QUANTITATIVE MEASUREMENTS

4.1 Contour length of impacting drops

Measuring the length of edges in digital images, such as the contour length of an impacting drop (e.g., Figure 3), requires first of all the identification of the edge of interest; in fact, edge detection algorithms find all edge features in an image (see e.g. Figure 5), including spurious edges inside the contour of the drop which must be erased.

The first step is to enhance all edges by checking the connectivity of pixels; in other words, if a pixel $p_{i,j}$ is surrounded by a sufficient number of pixels belonging to an edge, then $p_{i,j}$ must also belong to the same edge. In practice, this operation can be done by convolving the image with the kernel defined in Eq. (18), and replacing those pixels where the convolution product exceeds a certain threshold, k_2.

$$M_{FC} = \frac{1}{8}\begin{bmatrix} 1 & 1 & 1 \\ 1 & 0 & 1 \\ 1 & 1 & 1 \end{bmatrix} \tag{18}$$

Thus, if I_1 is the initial image containing edges, the new image after connectivity check is:

$$I_2 := \{I_1 * M_{FC} > k_2, \quad k_2 > 0.5\} \tag{19}$$

The hole filling procedure consists essentially in the same operation, but using a smaller value of the threshold, k_3:

$$I_3 := \{I_2 * M_{FC} > k_3, \quad k_3 < 0.5\} \tag{20}$$

Spurious edges can be removed by filling the area inside the drop contour line, i.e., by filling the pixels between the first and the last edge pixel of each row and each column, respectively. If the contour line is open, pixels must be filled on the side of spurious edges. Finally, the contour line is determined by applying the edge finding algorithm to the resulting binary image. Figure 7 shows the intermediate steps of the procedure applied to the drop image displayed in Figure 3.

The set of points $\{x_i, y_i\}$ constituting the contour of the wetted area (red points in Figure 7c) cannot be used directly to calculate the contour length because the set is unsorted; usually, conditional operations for matrices are performed in compilers first by rows and then by columns,

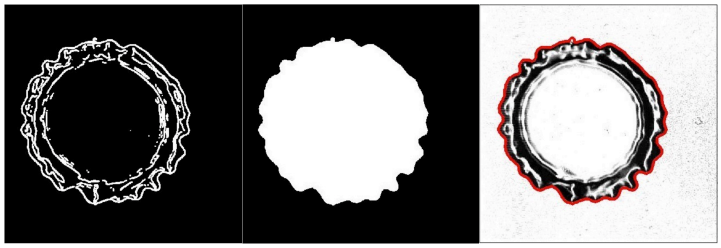

FIG. 7: Steps of contour line identification: (a) image edges after connectivity check ($k_2 = 0.6$) and hole filling ($k_3 = 0.1$); (b) spurious edges removal; (c) contour line (red) superimposed to the original image.

producing the set to be sorted by columns and then by rows. Ideally, the best way to sort the set is by growing angle in a polar coordinate system with origin inside the contour line, so that the pair $\{x_i, y_i\}$ can be converted to $\{\theta_i, r_i\}$. The origin $\{x_c, y_c\}$ of the polar coordinate system can be placed in the point with coordinates equal to the arithmetic mean of the contour line coordinates (Thoroddsen and Sakakibara, 1998):

$$x_c \equiv \overline{x} = \frac{1}{n}\sum_{i=1}^{n} x_i \quad , \quad y_c \equiv \overline{y} = \frac{1}{n}\sum_{i=1}^{n} y_i \tag{21}$$

where n is the total number of pixels belonging to the contour line. Alternatively, one can use the more accurate least squares fitting of circles (LSF circles) technique (Chernov and Lesort, 2005), which uses higher-order central moments of the contour line pixel coordinates:

$$\begin{bmatrix} \sum_{i=1}^{n} u_i{}^2 & \sum_{i=1}^{n} u_i v_i \\ \sum_{i=1}^{n} u_i v_i & \sum_{i=1}^{n} v_i{}^2 \end{bmatrix} \begin{bmatrix} x_c - \overline{x} \\ y_c - \overline{y} \end{bmatrix} = \frac{1}{2} \begin{bmatrix} \sum_{i=1}^{n} u_i{}^3 + \sum_{i=1}^{n} u_i{}^2 v_i \\ \sum_{i=1}^{n} v_i{}^3 + \sum_{i=1}^{n} u_i v_i{}^2 \end{bmatrix} \tag{22}$$

where $u_i = x_i - \overline{x}$ and $v_i = y_i - \overline{y}$. Once the centre of the wetted area is found, the variable change $\{x_i, y_i\} \rightarrow \{\theta_i, r_i\}$ is straightforward:

$$\theta_i = \alpha + \arctan\frac{y_i - y_c}{x_i - x_c} \quad , \quad r_i = \sqrt{(x_i - x_c)^2 + (y_i - y_c)^2} \tag{23}$$

where $\alpha = 0$ in the first quadrant, $\alpha = \pi$ in the second and third quadrants, and $\alpha = 2\pi$ in the fourth quadrant, respectively.

Figure 8 displays the contour line in polar coordinates, after sorting the pixels $\{\theta_i, r_i\}$ by growing θ_i. The contour line length, L, can now be obtained by simple numerical integration:

$$L = \int_0^{2\pi} r(\theta) d\theta \approx \sum_{i=0}^{n-1} (\theta_{i+1} - \theta_i) \frac{r_{i+1} + r_i}{2} \tag{24}$$

4.2 Dynamic contact angle of impacting drops

Angle measurements are relatively simple if the analytical expressions of the two intersecting edges are known, hence the abundance of edge fitting methods available in the literature. However, the optimal choice of the fitting curve and, in case of piecewise fitting, of partitions, are non-trivial issues that can be mitigated only at a high computational cost. An alternative approach

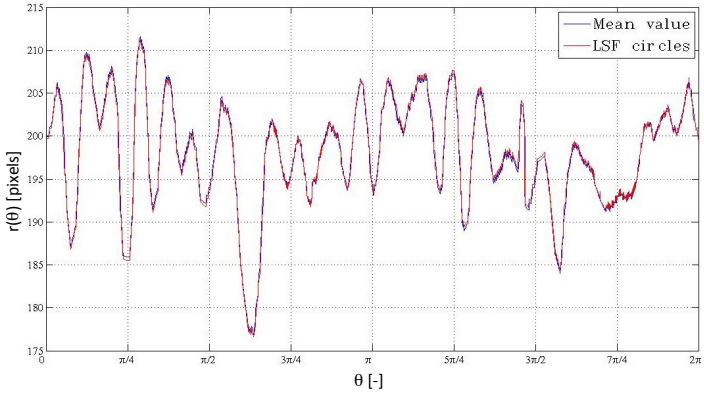

FIG. 8: Polar representation of the contour line of Figure 7c.

to measure angles (or more in general the slope of an edge) in digital images is to directly process the image intensity matrix without edge fitting.

An important example of angle measurement from images is the static or dynamic contact angle of a liquid drop in contact with a solid surface, as it appears in a side view image of the drop. The drop curvature causes non-uniform light scattering, which makes edge visualization difficult especially in the region of interest near the surface; thus, accurate contact angle measurements require high-quality images obtained with uniform, parallel back-to-front illumination. This is usually provided as a standard in commercial goniometers, however can be difficult to achieve in case of dynamic contact angle measurements (Bertola, 2010; Bertola and Wang, 2015), because high-speed cameras require a large illumination intensity and the drop curvature varies significantly during drop impact.

The exact position of the contact points where the drop edge meets the surface can be detected with the aid of the reflected image of the drop on the substrate, which is visualised by tilting the optical axis of the camera downwards at an angle α having a magnitude of a few degrees. This has two side effects: (i) the projected image of the substrate superimposes to the drop image in a thin strip containing the contact points, and (ii) the observed contact angle, θ_o, lies in a different plane than the actual contact angle, θ_a, introducing an error (usually negligible) that can be estimated by $\tan\theta_o = \tan\theta_a \cos\alpha$ (Chini et al., 2013).

A straightforward algortihm to compute contact angles from digital images (Biolè and Bertola, 2015b) is based on the univocal and monotonic relationship between the contact angle, θ, and the area of the overlapping region between the drop image and a suitable geometric shape (or *goniometric mask*) centered on the contact point, A, as illustrated schematically in Figure 9a. In particular, a triangular goniometric mask offers a number of advantages when discretised, including a weaker dependence of results on the mask size and a significantly lower computational cost. This happens because among all shapes that can be constructed inside a square matrix, the triangle is the convex shape enclosing the smallest number of elements, hence there are less non-zero elements involved in operations. Using an isosceles triangle having a base of lenght $2R$ and a height of length R as goniometric mask, and assuming it is small enough compared to the drop size that the portion of drop contour line inside it can be linearised, the relationship between the

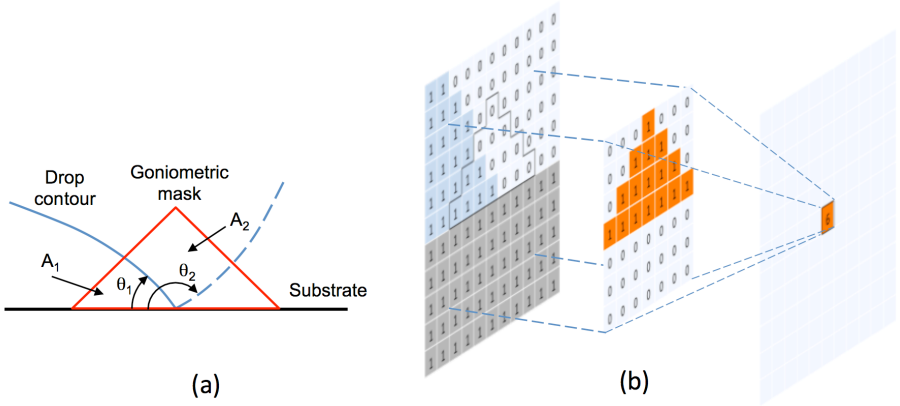

FIG. 9: Schematic of the relation between the contact angle and the overlapping area between the drop image and a triangle centered on the contact point (a), and schematic of the convolution between the drop image and the goniometric mask in the pixel corresponding to the contact point of the drop (b).

contact angle and the overlapping area is expressed by Eq. (25):

$$\theta = \frac{\pi}{2}(1+\lambda) + \arctan\frac{2A-(1+\lambda)R^2}{R^2-2A} \tag{25}$$

where $\lambda = -1$ for $A \leq R^2/2$ and $\lambda = 1$ for $A > R^2/2$.

In the case of binary images, the count of pixels falling within a certain delimited region is a direct measure of its area; thus, the area of the overlapping region sketched in Figure 9a can be obtained with a simple 2-dimensional convolution operation between the drop image matrix and a second binary matrix, defined in Eq. (26), corresponding to the image of a triangle, and centered on the pixel corresponding to the contact point in the drop image. To enable centring the mask on a single element (pixel), the mask size, i.e., the number of rows or column of the matrix, or the number of pixels of a side of the corresponding image, is $2b+1$, where b is an integer number. In fact, the discrete convolution operator between two matrices $\mathbf{A}$ and $\mathbf{B}$ yields a matrix whose elements, defined in Eq. (27), are the sums of the products of the elements of $\mathbf{A}$ and $\mathbf{B}$, as shown schematically in Figure 9b. Since convolution takes the rows and columns of the second matrix in reverse order, the goniometric mask must be flipped both vertically and horizontally.

$$M_G = \begin{pmatrix} 0 & 0 & 0 & \cdots & 0 & 0 & 0 \\ \vdots & \vdots & \vdots & & \vdots & \vdots & \vdots \\ 0 & 0 & 0 & \cdots & 0 & 0 & 0 \\ 1 & \cdots & \cdots & 1 & \cdots & \cdots & 1 \\ 0 & \ddots & & \vdots & & \iddots & 0 \\ \vdots & \ddots & \ddots & \vdots & \iddots & \iddots & \vdots \\ 0 & \cdots & 0 & 1 & 0 & \cdots & 0 \end{pmatrix} \tag{26}$$

$$A(r,c) = \sum_{i=0}^{2b}\sum_{j=0}^{2b} I(r-i, c-j) M_G(i,j) \tag{27}$$

The mask size, $z = 2b + 1$, strongly affects the angle measurement because a discrete mask can resolve a maximum number of discrete angle values equal to the number of pixels in the triangle, $(z + 1)^2/4$. Thus, the minimum value (in radians) that can be measured, corresponding to one pixel, is $4\pi/(z + 1)^2$; for example, to measure an angle of 1°, the mask size should be $z = 2\sqrt{180} - 1 \approx 25$. The overall accuracy of the method is the result of trade-off between the input parameters; on one hand, increasing the mask size pays back in terms of accuracy but, on the other hand, if the image size to mask size ratio is too small angles are not measurable. Accuracies comparable with those of average commercial software can be achieved with masks as small as 21×21 pixels, provided the image size to mask size ratio is ≥ 7.

In summary, the steps to obtain the contact angle value are:

- Convert the drop side view image into binary form using the procedure described in Section 4.1;
- Locate the position(s) $\{i_c, j_c\}$ of the contact point(s) using the procedure described in Section 3.2;
- Calculate the convolution between the drop image and the goniometric mask, $A = I * M_G$;
- Calculate the contact angle using the discrete version of Eq. (25):

$$\theta = \frac{\pi}{2}(1 + \lambda) + \arctan \frac{2A(i_c, j_c) - (1 + \lambda)(b + 1)^2}{(b + 1)^2 - 2A(i_c, j_c)} \tag{28}$$

The method can be easily adapted to measure contact angles on convex surfaces of arbitrary shape (Chen and Bertola, 2017).

A different approach to calculate the contact angle, which can be useful when edges in the image are ill-defined or blurred, is to consider all possible directions within a subset of the image around the contact point, as shown schematically in Figure 10a, and weigh them with the intensity gradient of the image (Biolè and Bertola, 2015a). Since the intensity gradient is maximum in correspondence of edges, the weighted average of directions corresponds to the tangent to the drop edge in the contact point hence enables finding the most likely value of the contact angle.

Setting the origin of the coordinate system in the contact point, directions are given by $m(x, y) = \arctan(y/x)$, therefore if I_S is a subset of the image around the contact point the weighted average angle is simply $\theta = ||\nabla I_S(x, y)|| * m(x, y)/||\nabla I_S(x, y)||$, where $*$ is the convolution operator. Although the concept is straightforward when the image intensity $I(x, y)$ and $m(x, y)$ are continuous functions, some further analysis is necessary if the image is a discrete matrix of pixels, $I_{i,j}$. In this case, the discrete matrix of directions can be written as $m_{i,j} = \arctan[(i - i_c)/(j - j_c)]$, where i_c and j_c are, respectively, the row and column of the central element of the matrix $m_{i,j}$.

$$m_{i,j}^{5\times5} = \begin{pmatrix} 45 & 63.43 & -90 & -63.43 & -45 \\ 26.56 & 45 & -90 & -45 & -26.56 \\ 0 & 0 & NaN & 0 & 0 \\ -26.56 & -45 & 90 & 45 & 26.56 \\ -45 & -63.43 & 90 & 63.43 & 45 \end{pmatrix} \tag{29}$$

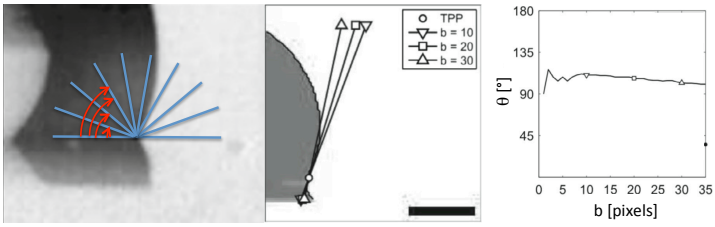

FIG. 10: Contact angle measurement using the probabilistic approach: (a) original ill-defined drop image; (b) most likey tangent lines obtained for three different values of the directional matrix half-size, $b = (z-1)/2$; (c) dependence of the measured contact angle on the directional matrix half-size.

As one can see in the example given in Eq. (29), which shows the explicit values of $m_{i,j}$ for a 5×5 matrix, each value (corresponding to a particular angular direction, except the central element) appears a certain number of times, $n_{i,j}$; if z denotes the size of $m_{i,j}$, then $2 \leq n_{i,j} \leq z$. Thus, each element of $m_{i,j}$ must be divided by its probability density, $P_{i,j} = n_{i,j}/N$, where $N = z^2 - 1$ is the number of angular directions in $m_{i,j}$ (i.e., the number of elements of $m_{i,j}$ excluding the central one). This is equivalent to multiply each element of $m_{i,j}$ by the corresponding element of a normalized weighing matrix defined as:

$$W_{i,j} = \frac{\frac{1}{P_{i,j}} - (\frac{1}{P_{i,j}})_{min}}{(\frac{1}{P_{i,j}})_{max} - (\frac{1}{P_{i,j}})_{min}} = \frac{\frac{N}{n_{i,j}} - \frac{N}{z}}{\frac{N}{2} - \frac{N}{z}} = \frac{\frac{z}{n_{i,j}} - 1}{\frac{z}{2} - 1} \tag{30}$$

Finally, the most likely value of the contact angle is given by:

$$\theta = \left[\frac{||\nabla I_{i,j}|| * (W_{i,j} \cdot m_{i,j})}{||\nabla I_{i,j}|| * W_{i,j}} \right]_{i=i_c, j=j_c} \tag{31}$$

where i_c and j_c are, respectively, the row and column of the pixel corresponding to the contact point. An example of contact angle measurement using this method, and of the measurement sensitivity to the directional mask size, is shown in Figure 10.

5. CASE STUDY

This section provides an example of application of the image processing protocol outlined above to the analysis of high-speed movies of impacting drops. In particular, the impact of water drops onto a hydrophobic substrate (a glass slide coated with Parafilm-M, with equilibrium contact angle of $\approx 90°$) was recorded using a Vision Research Phantom V9.17 high-speed camera, at a rate of 5,000 frames per second, with exposure time of 190µs and a resolution of 576×576 pixels. Drops were released from a blunt hypodermic needle suspended above the substrate at the distances of 20 mm, 60 mm, 100 mm, and 140 mm, corresponding to impact velocities, $U_0 = \sqrt{2g(h - D_0)}$ (where h is the falling height and D_0 the equilibrium drop diameter) equal to 0.58 m/s, 1.06 m/s, 1.38 m/s, and 1.64 m/s. Accordingly, the impact Weber numbers were $We = 14$, $We = 47$, $We = 80$, and $We = 113$. The equilibrium drop diameter was calculated as $D_0 = \sqrt[3]{6m/\pi\rho} = 3.06 \pm 0.05$ mm, where the drop mass, m, was determined using a precision scale (Mettler PM100).

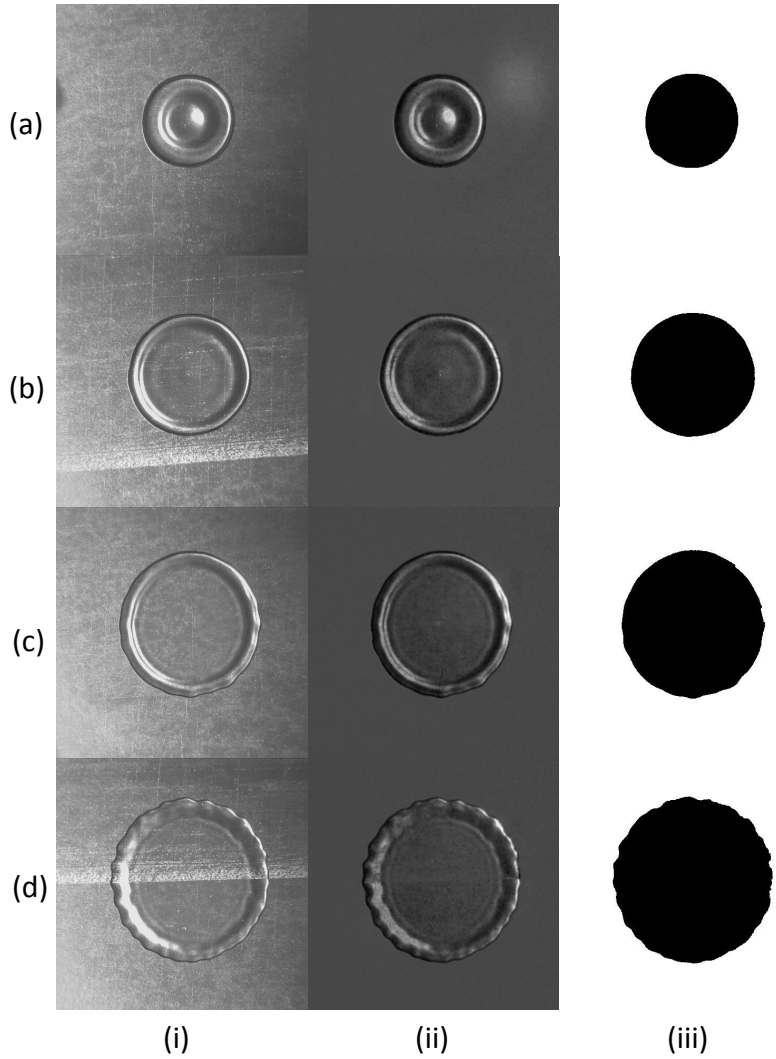

FIG. 11: Images of water drops at maximum spreading after impact on a glass slide coated with Parafilm-M, for impact Weber numbers $We = 14$ (a), $We = 47$ (b), $We = 80$ (c), $We = 113$ (d), at different stages of the image processing protocol: (i) raw image; (ii) image after background subtraction, equalization, and Gaussian smoothing; (iii) binary image defining the contour line.

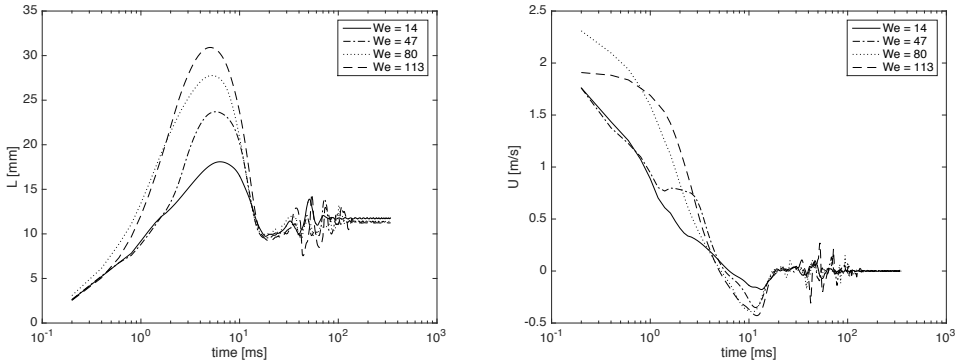

FIG. 12: Contact line length (a) and velocity (b) measured as a function of time at different impact Weber numbers.

In the case of the contact line perimeter measurement, the camera and the lens were aligned vertically under the drop target, looking through the semi-transparent substrate, while in the case of contact angle measurements the optical axis was aligned parallel to the substrate to obtain side views of the drops. Further details about the experimental setup and procedure can be found in Biolè and Bertola (2015c) and Bertola and Wang (2015).

Figure 11 displays images of impacting drops at maximum spreading, for different impact Weber numbers, at different stages of image processing. In particular, Figures 11(i),(a-d) display the raw images as obtained from the camera, Figures 11(ii),(a-d) display the same images image after background subtraction, histogram equalization, and Gaussian smoothing, and Figures 11(iii),(a-d) display the binary output defining the contour line. The contact line length, L, calculated according to Eq. (24), and the average contact line velocity calculated as:

$$U_{i+1} = \frac{L_{i+1} - L_i}{t_{i+1} - t_i} \tag{32}$$

where i is the discrete time, are shown in Figures 12a and 12b, respectively.

Dynamic apparent contact angle measurements were obtained from side view images of impacting drops, a selection of which is displayed in Figure 13 for the four impact Weber numbers considered. After making contact with the surface, the drop starts to spread and deforms initially taking the shape a pancake, which rapidly evolves into a thin liquid disk (the lamella) surrounded by a toroidal rim. After maximum spreading, the drop recoils and eventually attains the equilibrium spherical cap shape after several seconds.

The apparent dynamic contact angles are plotted as a function of time in Figure 14a, for the four impact Weber numbers considered. Initially, the apparent contact angle rapidly decreases from the initial value of 180° at the moment of impact and goes through a minimum in less than 1 ms, then it grows to reach approximately the value of the advancing contact angle until maximum spreading. During the receding phase, contact angles exhibit amplitude oscillations that exponentially decay until they attain the equilibrium value (approximately 95°) after several seconds.

In general, dynamic contact angle time series are affected by an algorithmic noise significantly higher than length measurements, therefore it may be necessary to smooth data using a

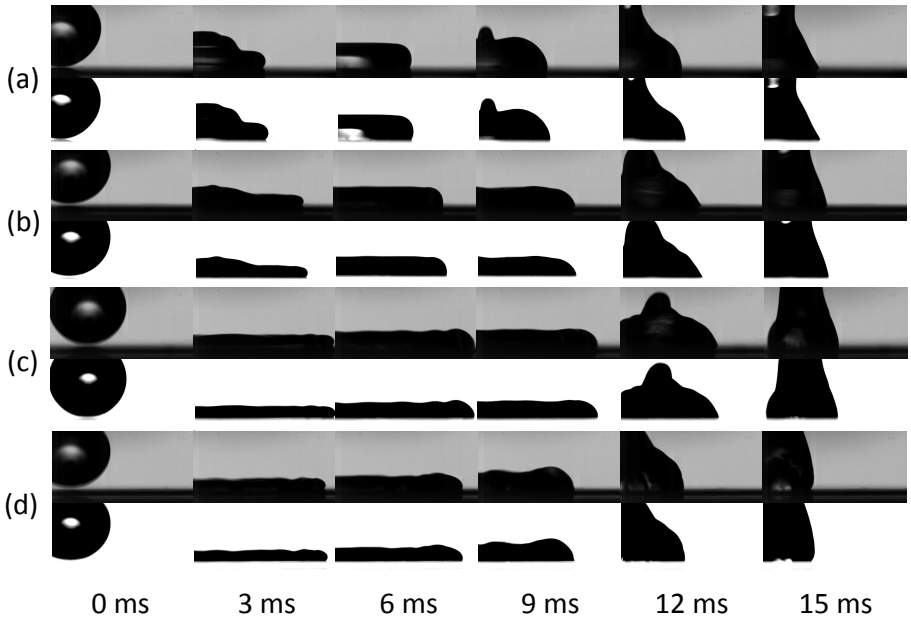

FIG. 13: Side view images of water drops impacting on a glass slide coated with Parafilm-M, for impact Weber numbers $We = 14$ (a), $We = 47$ (b), $We = 80$ (c), $We = 113$ (d): raw images (odd rows); processed images (even rows).

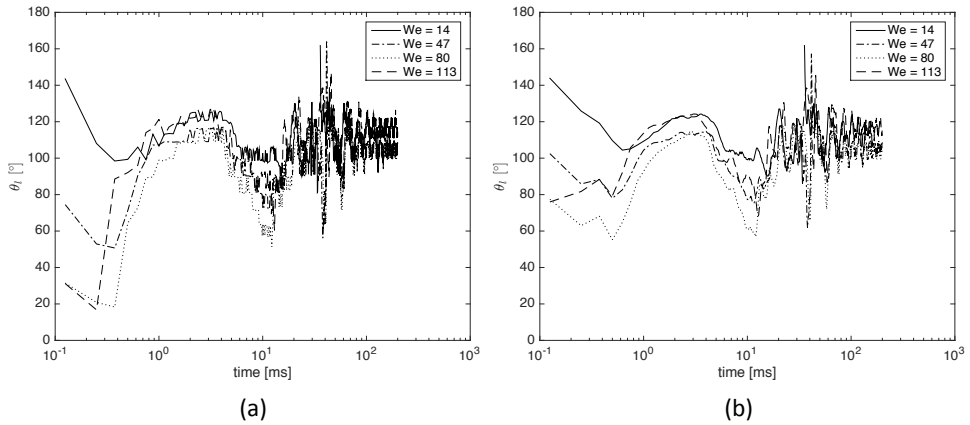

FIG. 14: Apparent dynamic contact angles measured as a function of time at different impact Weber numbers. (a) Original measurements; (b) smoothed data by moving average over 1 ms.

moving average filter, as shown in Figure 14b. This operation, however, reduces the time resolution, and consequently the accuracy of measurements during the spreading stage, where the largest gradients are observed.

6. CONCLUSIONS

A systematic approach to obtain comprehensive quantitative measurements from digital images of impacting drops is discussed and recast into formal mathematical terms. The procedure consists of: (i) an initial pre-processing, which includes image enhacement and background removal; (ii) detection of singular features, i.e. edges and corners; (iii) measurement of contour lengths; (iv) measurement of contact angles.

The use of a standard, automated procedure instead of customized image processing or, even worse, manual measurements with commercial software, which heavily depend on the operator's skills, on one hand improves the quality and consistency of measurements, and on the other hand enables more reliable comparisons among different experimental data sets.

Whilst the proposed image processing procedure maximizes the quality of data that can be extracted from a given image, the quality of the raw image determined by the optical setup remains the most important factor to obtain accurate quantitative measurements.

REFERENCES

Bateni, A., Susnar, S., Amirfazli, A., and Neumann, A., A high-accuracy polynomial fitting approach to determine contact angles, *Colloids and Surfaces A: Physicochemical and Engineering Aspects*, vol. **219**, no. 1, pp. 215 – 231, 2003.

Bertola, V., Effect of polymer additives on the apparent dynamic contact angle of impacting drops, *Colloids and Surfaces A Physicochemical and Engineering Aspects*, vol. **363**, no. 1-3, pp. 135–140, 2010.

Bertola, V. and Wang, M., Dynamic contact angle of dilute polymer solution drops impacting on a hydrophobic surface, *Colloids and Surfaces A: Physicochemical and Engineering Aspects*, vol. **481**, pp. 600–608, 2015.

Biolè, D. and Bertola, V., The fuzzy interface of a drop, *Computing and Visualization in Science*, vol. **17**, no. 1, pp. 19–32, 2015a.

Biolè, D. and Bertola, V., A goniometric mask to measure contact angles from digital images of liquid drops, *Colloids and Surfaces A: Physicochemical and Engineering Aspects*, vol. **467**, pp. 149–156, 2015b.

Biolè, D. and Bertola, V., The role of the microscale contact line dynamics in the wetting behaviour of complex fluids, *Archives of Mechanics*, vol. **67**, no. 5, pp. 401–414, 2015c.

Biolè, D., Wang, M., and Bertola, V., Assessment of direct image processing methods to measure the apparent contact angle of liquid drops, *Experimental Thermal and Fluid Science*, vol. **76**, pp. 296–305, 2016.

Canny, J., A computational approach to edge detection., *IEEE transactions on pattern analysis and machine intelligence*, vol. **8**, no. 6, pp. 679–698, 1986.

Chen, S. and Bertola, V., Drop impact on spherical soft surfaces, *Physics of Fluids*, vol. **29**, no. 8, p. 082106, 2017.

Chernov, N. and Lesort, C., Least squares fitting of circles, *Journal of Mathematical Imaging and Vision*, vol. **23**, no. 3, pp. 239–252, 2005.

Chini, S., Bertola, V., and Amirfazli, A., A methodology to determine the adhesion force of arbitrarily

shaped drops with convex contact lines, *Colloids and Surfaces A: Physicochemical and Engineering Aspects*, vol. **436**, pp. 425–433, 2013.

Chini, S.F. and Amirfazli, A., A method for measuring contact angle of asymmetric and symmetric drops, *Colloids and Surfaces A: Physicochemical and Engineering Aspects*, vol. **388**, no. 1-3, pp. 29–37, 2011.

Harris, C. and Stephens, M., A combined corner and edge detector, *Proceedings of the Alvey Vision Conference*, Alvety Vision Club, pp. 23.1–23.6, 1988, doi:10.5244/C.2.23.

Hoorfar, M. and Neumann, A.W., Recent progress in axisymmetric drop shape analysis (adsa), *Advances in Colloid and Interface Science*, vol. **121**, no. 1, pp. 25–49, 2006.

Hutchings, I.M., Martin, G., and Hoath, S.D., High Speed Imaging and Analysis of Jet and Drop Formation, *Journal of Imaging Science and Technology*, vol. **51**, no. 5, pp. 438–444, 2007.

Kitchen, L. and Rosenfeld, A., Gray-level corner detection, *Pattern Recognition Letters*, vol. **1**, no. 2, pp. 95–102, 1982.

Langridge, D., Curve encoding and the detection of discontinuities, *Computer Graphics and Image Processing*, vol. **20**, no. 1, pp. 58–71, 1982.

Lindeberg, T., Discrete derivative approximations with scale-space properties: A basis for low-level feature extraction, *Journal of Mathematical Imaging and Vision*, vol. **3**, no. 4, pp. 349–376, 1993.

Lindeberg, T., Edge detection and ridge detection with automatic scale selection, *Proceedings CVPR IEEE Computer Society Conference on Computer Vision and Pattern Recognition*, pp. 465–470, 1996.

Lindeberg, T., Edge detection and ridge detection with automatic scale selection, *International Journal of Computer Vision*, vol. **30**, no. 2, pp. 117–156, 1998.

Marr, D. and Hildreth, E., Theory of edge detection., *Proceedings of the Royal Society of London. Series B*, vol. **207**, no. 1167, pp. 187–217, 1980.

Mokhtarian, F. and Suomela, R., Robust image corner detection through curvature scale space, *IEEE Transactions on Pattern Analysis and Machine Intelligence*, vol. **20**, no. 12, pp. 1376–1381, 1998.

Moravec, H.P., Obstacle Avoidance and Navigation in the Real World by a Seeing Robot Rover, PhD thesis, Stanford, CA, USA, 1980. AAI8024717.

Noble, J.A., Finding corners, *Proceedings of the Alvey Vision Conference*, Alvety Vision Club, pp. 37.1–37.8, 1987, doi:10.5244/C.1.37.

Perona, P. and Malik, J., Scale-space and edge detection using anisotropic diffusion, *IEEE transactions on pattern analysis and machine intelligence*, vol. **12**, pp. 629–639, 1990.

Rioboo, R., Tropea, C., and Marengo, M., Outcomes from a drop impact on solid surfaces, *Atomization and Sprays*, vol. **11**, no. 2, 2001.

Rotenberg, Y., Boruvka, L., and Neumann, A., Determination of surface tension and contact angle from the shapes of axisymmetric fluid interfaces, *Journal of Colloid and Interface Science*, vol. **93**, no. 1, pp. 169–183, 1983.

Rutkowski, W.S. and Rosenfeld, A., A comparison of corner detection techniques for chain coded curves, Tech. Rep. 623, University of Maryland, 1978.

Schuetter, S.D., Shedd, T.A., Doxtator, K., Nellis, G.F., Peski, C.K.V., Grenville, A., Lin, S.H., and Owe-Yang, D.C., Measurements of the dynamic contact angle for conditions relevant to immersion lithography, *Journal of Micro/Nanolithography, MEMS, and MOEMS*, vol. **5**, pp. 5–9, 2006.

Smith, S. and Brady, J., Susan–a new approach to low level image processing, *International Journal of Computer Vision*, vol. **23**, pp. 45–78, 1997.

Sobel, I. and Feldman, G., An isotropic 3x3 image gradient operator, *Pattern Classification and Scene Analysis*, Duda, R. and Hart, P. (Eds.), John Wiley and Sons, pp. 271–272, 1968.

Stalder, A., Kulik, G., Sage, D., Barbieri, L., and Hoffmann, P., A snake-based approach to accurate determination of both contact points and contact angles, *Colloids and Surfaces A: Physicochemical and Engineering Aspects*, vol. **286**, no. 1, pp. 92–103, 2006.

Thoroddsen, S., Etoh, T., and Takehara, K., High-Speed Imaging of Drops and Bubbles, *Annual Review of Fluid Mechanics*, vol. **40**, no. 1, pp. 257–285, 2008.

Thoroddsen, S.T. and Sakakibara, J., Evolution of the fingering pattern of an impacting drop, *Physics of Fluids*, vol. **10**, no. 6, p. 1359, 1998.

Torre, V. and Poggio, T., On Edge Detection, *IEEE transactions on pattern analysis and machine intelligence*, vol. **2**, pp. 147–163, 1986.

Versluis, M., High-speed imaging in fluids, *Experiments in Fluids*, vol. **54**, no. 2, p. 1458, 2013.